Device

CellPress

Review

Advances and challenges in microdisplays and imaging optics for virtual reality and mixed reality

Zhiyong Yang,[1] Zhenyi Luo,[1] Yuqiang Ding,[1] Yizhou Qian,[1] Sung-Chun Chen,[2] Chih-Lung Lin,[2] and Shin-Tson Wu[1,*]
[1]College of Optics and Photonics, University of Central Florida, Orlando, FL 32816, USA
[2]Department of Electrical Engineering, National Cheng Kung University, Tainan 701, Taiwan
*Correspondence: swu@creol.ucf.edu
https://doi.org/10.1016/j.device.2024.100398

THE BIGGER PICTURE The recent launches of Apple Vision Pro and Meta Quest 3 have shown the broadening market appeal for what was once considered a niche product for tech enthusiasts. However, these headsets still pose high barriers of entry for consumers due to their bulkiness, high price, and short battery life. A virtual-reality (VR) and pass-through mixed-reality (MR) headset should have a wide field of view, crisp image, compact formfactor, light weight, wide color gamut, and low power consumption. These demands require technology and material design far beyond the already impressive achievement in traditional direct-view display light engines and viewing optics in the past few decades, such as those used in smartphones and flat screen TVs. To address these challenges, numerous approaches have been proposed and developed. In this review, we discuss high-efficiency and compact architectures of microdisplays and viewing optics to guide the future development direction of these devices.

SUMMARY

In this review, we discuss emerging approaches to advance virtual-reality (VR) displays in the following criteria: field of view (FoV), resolution density, formfactor, color gamut, and optical efficiency. To improve the resolution density and optical efficiency, two display technologies, field-sequential-color liquid-crystal displays (LCDs) with suppressed color breakup and tandem micro-organic light-emitting diodes (OLEDs), are under active development. While white micro-OLEDs can provide a high resolution density, the use of color filters dramatically decreases the optical efficiency. RGB micro-OLEDs can achieve a higher efficiency but face their own set of challenges in manufacturing. The amalgamation of these technical demands also creates additional challenges. For example, to achieve a wide FoV with a small display size requires a small f-number imaging lens; thus, a delicate optical system design is needed to mitigate the aberrations. We also discuss four main architectures of the viewing optics; i.e., Fresnel optics and three types of pancake lens: traditional, double-path, and Faraday rotator-based lens.

INTRODUCTION

With the prevalence of real-time pass-through video feedback in virtual-reality (VR) headsets, the capabilities of these devices are being expanded to also include mixed-reality (MR) experiences.[1] Full-color and high-resolution video pass-through enable a seamless transition from a fully immersive VR to MR, which allows the user to interact with the real world while wearing the headset, as Figure 1A depicts. As demonstrated by the Apple Vision Pro launched earlier this year, developers are also looking to provide reverse video pass-through with an external display to allow others to see the user's face. Although a great deal of progress has been made in the commercialization and market adaptation of VR devices in the past decade, there is still a huge gap between the current technology and what most consumers would like to see, which is a device that shapes and weighs about the same as a pair of glasses[2] and can provide a wide field of view (FoV), crisp image, and has a long battery life with an affordable price tag. Therefore, there are plenty of opportunities for improvement and innovation in the fields of microdisplays and imaging optics. For example, tailoring the angular radiation pattern of the display panel helps to maximize the optical efficiency because any light output that does not end up inside the pupil is wasted, as explained in Figure 1A.

This review seeks to provide an overview on recent advances and remaining challenges toward a better VR device. We will

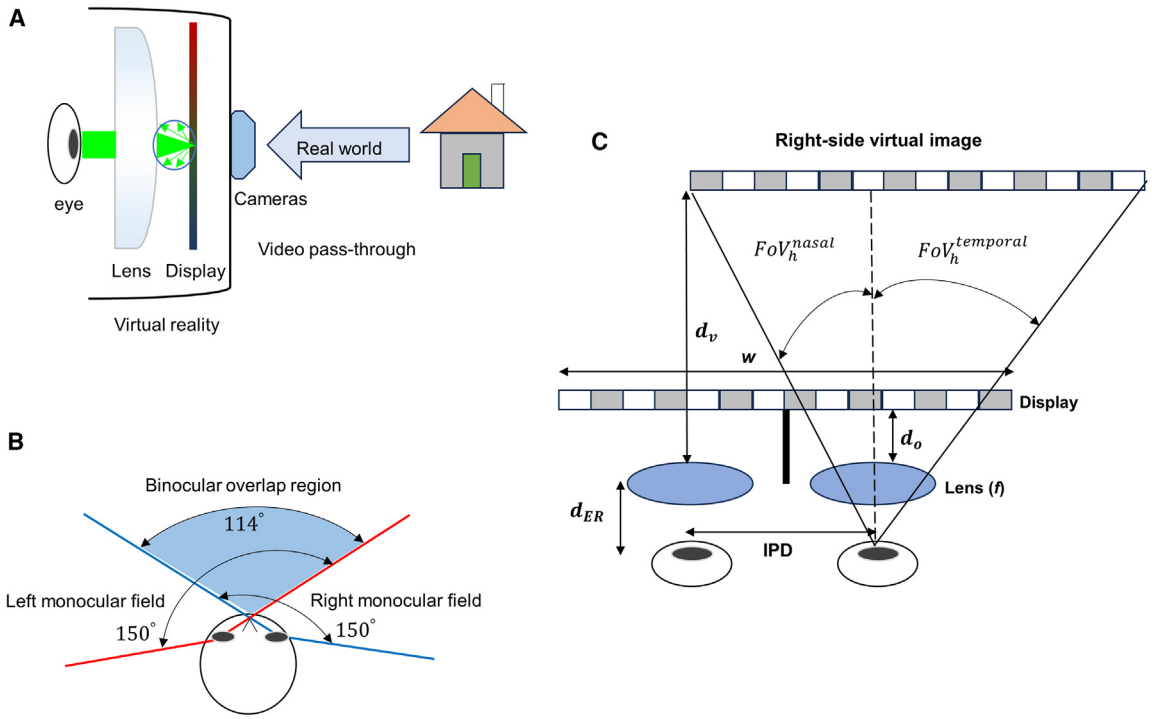

Figure 1. Schematics of VR, MR, and FoV

(A) Working principle of VR and video pass-through MR.

(B) FoV of human vision.

(C) FoV related to ER and IPD in a real VR system.

briefly discuss pivotal performance requirements, including FoV, resolution density, aperture ratio, and motion blur. We will also discuss how the FoV correlates with the panel size, inter-pupillary distance (IPD), and eye relief (ER; the distance between the user's eye and the imaging optics). Next, we will compare two main VR light engines, i.e., the high-pixels-per-inch (PPI) active-matrix liquid-crystal display (AMLCD) used in Meta Quest 3, Pico 4 Pro, and HTC Vive Pro 2, and the organic light-emitting diode on silicon (OLEDoS; also called micro-OLED) used in Apple Vision Pro. Advanced display architectures such as microcavity tandem OLEDs and novel driving algorithms of mini-LED backlit field-sequential-color (FSC) AMLCDs will also be discussed. For viewing optics, recent optical architectures such as double-path pancake lens and theoretically lossless Faraday rotator-enabled pancake lens will be highlighted.

Definitions of performance metrics

The FoV is referred to as the angular extent of an image visible to the eyes. The definition of horizontal binocular FoV is inconsistent in the literature because it can refer to either the range that is visible to both eyes (known as binocular overlap FoV) or the range that is visible to at least one eye (known as total monocular FoV). In this review, we define the horizontal FoV as the latter, which VR headsets typically quote. Under this definition, the horizontal FoV for a pair of human eyes is about 200°, with a binocular overlap FoV of about 114° and a single-eye horizontal FoV of about 150°, as schematized in Figure 1B. Commercial VR headsets such as Meta Quest Pro support a horizontal FoV of ~106° and a single-eye horizontal FoV of ~90°.

In a VR system, the single-eye FoV can be derived as shown below:

$$\text{FoV} \approx 2 \times tan^{-1}\left(\frac{D/2}{f}\right), \qquad \text{(Equation 1)}$$

where D is the panel size and f is the effective focal length of the compound viewing lenses. The relationship illustrated by Equation 1 highlights the challenge to achieving a large FoV with a small microdisplay panel. For example, Apple Vision Pro adopts two 1.4-inch micro-OLED panels (one for each eye). To achieve a single-eye horizontal FoV of 90°, one needs f-number = 0.5 (or numerical aperture [NA] = 0.7) under the assumption that the aperture size of optical lenses is same as the display panel. Such a small f-number dictates a sophisticated design of viewing optics to mitigate aberrations. A more accurate calculation of FoV should also consider IPD and ER, as illustrated in Figure 1C. The IPD variance across the world's population is from 51 to 71 mm. Therefore, the distance between two magnifying lenses can be set at an average IPD of ~61 mm.

According to Figure 1C, FoV_h^{nasal} and $FoV_h^{temporal}$ can be expressed as follows:

$$FoV_h^{nasal} = tan^{-1}\left(\frac{IPD/2}{d_v+d_{ER}}\frac{f}{f-d_o}\right), \qquad \text{(Equation 2)}$$

$$FoV_h^{temporal} = tan^{-1}\left(\frac{w/2 - IPD/2}{d_v + d_{ER}}\frac{f}{f - d_o}\right), \quad \text{(Equation 3)}$$

where d_v is the distance from the virtual image to the lens, d_{ER} is the ER distance, f is the effective focal length, d_o is the distance from the display panel to the lens, and w is the horizontal panel width. Furthermore, the single-eye horizontal FoV is the sum of FoV_h^{nasal} and $FoV_h^{temporal}$, the binocular overlap FoV is $2FoV_h^{nasal}$, and the horizontal FoV is $2FoV_h^{temporal}$. According to Equations 2 and 3, a smaller IPD leads to a smaller binocular overlap and a larger difference between the horizontal FoV and the single-eye horizontal FoV. On the other hand, although a larger ER allows for the insertion of correction lens, the FoV becomes smaller.

To reproduce crispy images without the screen-door effect (referring to the noticeable pixel structure including black matrices), high resolution density is critical. To achieve 60 pixels per degree (PPD) (i.e., 1 arcmin of visual acuity) and a single-eye horizontal FoV of 100°, 6,000 horizontal pixels should be packed in each display panel. For transmissive AMLCDs, such a high resolution density leads to a diminishing aperture ratio (i.e., the ratio of transmission area to the total pixel area). A small aperture ratio increases the power consumption and causes undesirable thermal effects. Compared to a high-PPI transmissive AMLCD, reflective liquid crystal on silicon (LCoS) exhibits a much higher aperture ratio (~90%) and resolution density (>6,000 PPI with pixel size ≤ 4 μm) because of the reflective operation and the silicon backplane,[3,4] thus contributing to unnoticeable screen-door effect. But its formfactor is usually larger than that of the transmissive AMLCD owing to its bulkier illumination optics. Such an increased formfactor is undesirable to VR/MR headsets, unless a more compact illumination system can be developed. Similar to LCoS, micro-OLED adopts a silicon backplane to achieve high resolution density and top-emitting mechanism to enlarge the aperture ratio.[5] Such an emissive micro-OLED possesses a more compact formfactor and higher native contrast ratio than LCoS.

Besides high resolution density and high aperture ratio, motion blur is another important metric to evaluate the capability of displaying fast-moving objects. To mitigate motion artifacts, a low (10%–20%) persistence can be introduced. This persistence is also called duty ratio, which refers to the ratio of the backlight-on time to the frame time. However, a low persistence together with a low-efficiency pancake lens would demand a high-luminance light engine. For example, to deliver 300 nits to human eyes in a VR headset, the light engine with 25,000 nits is needed, assuming 10% persistence and 12% optical efficiency of the pancake lens. Such a high luminance poses a challenge to micro-OLEDs (e.g., the compromised lifetime). According to the above analyses, further developments on display and optics are urgently needed. In the following, we review recent advancements and challenges of AMLCDs, micro-OLEDs, and various architectures of viewing optics.

AMLCDs

LCD is a non-emissive display produced on glass substrates and AMLCD adopts thin-film transistors (TFTs) to switch the desired pixels and storage capacitors to hold the charge until the next refresh cycle. Although AMLCD has existed as a direct-view display for about half a century, VR poses harsher requirements that demand the development of next-generation high-resolution-density AMLCDs integrated with mini-LED backlight. Presently, the state-of-the-art resolution density of AMLCDs is 2,117 PPI as demonstrated by BOE and Innolux.[6] However, a much higher resolution density is needed because it helps eliminate the screen-door effect and enables high-resolution light-field displays[7] to alleviate the vergence-accommodation conflict. For example, the required PPI is about 3,760 to achieve 60 PPD and a single-eye horizontal FoV of 100° with a 2.2-inch square AMLCD.

Color-filter-based AMLCDs

In color-filter-based AMLCDs, a white LED backlight produced by blue LEDs and color converters is commonly used. The white light travels through the liquid crystal (LC) layer and RGB color filters to generate spatial color mixing, as schematized in Figure 2A. In this way, a pixel consists of three side-by-side RGB subpixels. The full width at half maximum (FWHM) of quantum dots (QDs) is narrower than that of the emitted spectra of micro-OLEDs, as a result, Meta Quest Pro adopting mini-LED backlight and QD color conversion film exhibits a wider color gamut (100% DCI-P3) than Apple Vision Pro (92% DCI-P3). Meanwhile, to increase contrast ratio and reduce power consumption,[8] a mini-LED backlight array with local dimming zones has been used. Despite the native high contrast ratio of emissive displays such as micro-OLEDs and micro LEDs,[9] the mini-LED backlit LCD may exhibit an overall higher system contrast ratio because modulating the luminance or angular distribution in certain zones helps reduce stray light in the pancake optics system.[10] In the following paragraphs, we will briefly illustrate how driving circuits and color converters play critical roles to the performance of advanced AMLCDs.

The driving circuits of AMLCDs exist in the mini-LED backlight, LC pixel circuits, and peripheral circuits such as the gate driver and the source driver. The mini-LEDs of each local dimming zone are controlled by the driving current to generate the gray levels of the backlight. For pixel circuits, when the scan signal turns on the switching TFTs, the LCs are reorientated by the data voltage from the source driver integrated circuit (IC). Then the scan signal turns off to prevent the influence of the data line while the other rows of pixels are addressed, and the data voltage is maintained by the storage capacitor. For peripheral circuits, gate-on-array (GOA) circuits are used to generate the square waveforms for scan signals because they can exhibit a more compact structure and lower cost than the previous gate driver IC.[11]

The components of driving circuits comprise of low-temperature polycrystalline silicon (LTPS) TFTs and indium gallium zinc oxide (IGZO) TFTs. LTPS TFTs have higher mobility and current driving capability, so they are more suitable for driving the mini-LEDs to generate high luminance.[12] Owing to their threshold voltage variations and large leakage currents, the luminance nonuniformity needs to be compensated by the circuit designs widely used in emissive displays or by optical films such as diffusers. LTPS TFTs are also suitable for the GOA circuit[13] since

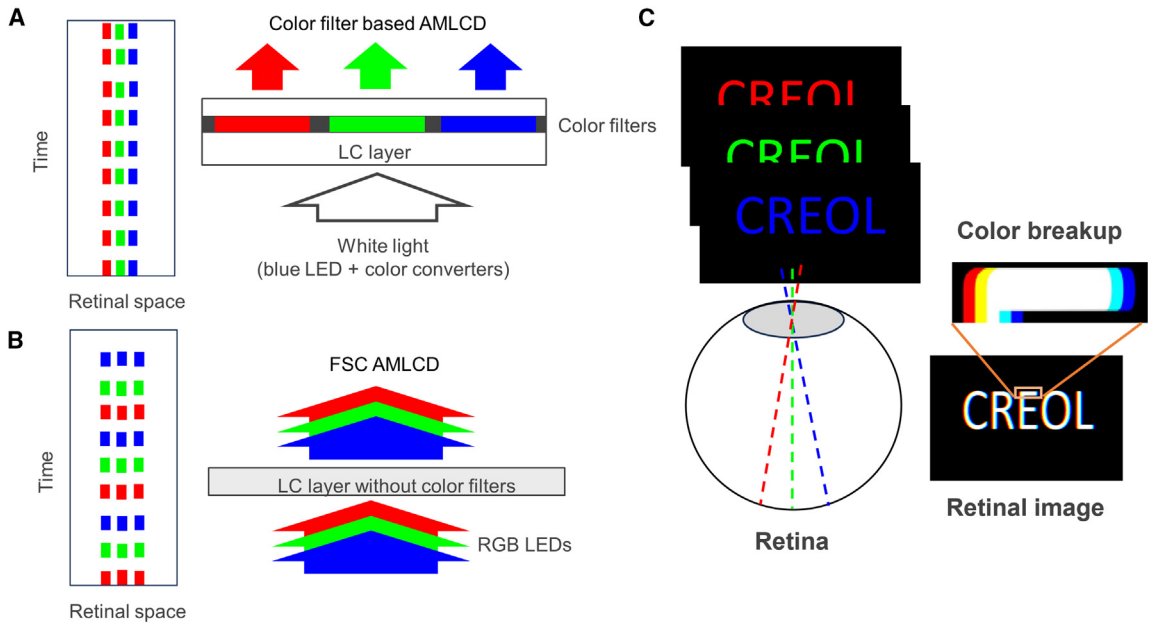

Figure 2. AMLCDs used for VR/MR displays

(A) Working principle of color-filter-based AMLCDs.

(B) Working principle of FSC AMLCDs.

(C) CBU issue arising from a relative movement between flashing subframes and human eyes.

a large current can be generated by the pull-up/down TFTs to charge or discharge the scan lines fast. With reduced rising or falling time, a close-to-ideal square waveform for the scan lines can be generated by GOA. Compared to LTPS TFTs, IGZO TFTs exhibit more uniform threshold voltages, smaller leakage currents, and lower costs, which are more suitable for the high-PPI LC pixel circuits.[14] This is because, when the pixel size is decreased, the storage capacitor will be smaller to ensure decent aperture ratio, but the data voltage is more easily affected by the leakage current. To reduce the leakage current, the dual gate structure[15] or lightly doped drain[16] is required in the LTPS TFT, inevitably increasing the TFT size and constraining the PPI. For the above-mentioned reasons, Meta Quest 3 adopted the hybrid backplane: the LC pixel circuits use IGZO TFTs to achieve 1,218 PPI, while the GOA circuits use LTPS TFTs to generate improved square waveforms for scan signals.

In addition to high PPI, high resolution (e.g., 6,000 per eye) poses another challenge to scanning time. To leave enough time for writing the data voltage from the source driver IC, the rising/falling time of the waveform generated by the GOA circuit should be reduced. Besides using LTPS TFTs for the GOA circuit, such as in Meta Quest 3, circuit designs help reduce the rising/falling time. For example, the two-step-bootstrapping method[17] has been proposed to increase the voltage of the gate node of pull-up/down TFTs and thus reduce the rise/fall time. By dividing the panel into two halves, the parasitic resistance and capacitance of the scan line are both halved, and the rising/falling time of the waveform can be further reduced because of the reduced RC (Resistor-Capacitor) time constant.[18] Another way is to separate the scan lines of odd and even rows into the left and right side of the panel, respectively.[19] The layout area for each row of GOA is then doubled, so the pull-up/down TFTs can be larger to enable a higher charging capability.

Phosphor color converters in white LEDs can possess a high quantum yield (~90%) and excellent stability. Owing to more saturated color and increased transmittance through color filters, combing red and green phosphors with blue LEDs is a better option than using yttrium aluminum garnet (YAG)-based yellow phosphors. In 2020, GE research team announced green Eu^{2+} phosphors with an FWHM < 35 nm and KSF ($K_2SiF_6:Mn^{+4}$) red phosphor to cover 88% Rec. 2020 color gamut.[20] Currently, the phosphor particle size can be reduced to submicrometer, but the main challenge of applying phosphors on mini-LEDs is that the luminous efficiency of phosphor is proportional to its particle size.[21] Compared to phosphors, QDs can provide a more vivid color and better uniformity due to the small particle size, high photoluminescence quantum yield (PLQY), high blue-light absorbance, and narrow emission-spectrum bandwidth.[22] For this reason, Meta Quest Pro equipped with QDs can exhibit a 30% wider color gamut than Meta Quest 2, which uses edge-lit phosphor-converted white LEDs.

Toxicity, thermal stability, and chemical stability are some of the main concerns for current QD materials. To avoid toxicity, Cd-free QDs such as InP and perovskite QDs (PeQDs) are rapidly developing. In 2020, a green and red dual-emissive PeQD was developed, and the integration of the dual-emissive films with blue mini-LEDs boosts the color gamut to ~130% NTSC.[23] The PLQY for green and red PeQDs is 95% and 86%, respectively.[23] To increase stability, remote core/shell QDs with proper sealing are preferred instead of on-chip QDs. The stability of PeQDs is even worse than CdSe- or InP-based QDs because of the ionic nature. To overcome this issue, strategies such as

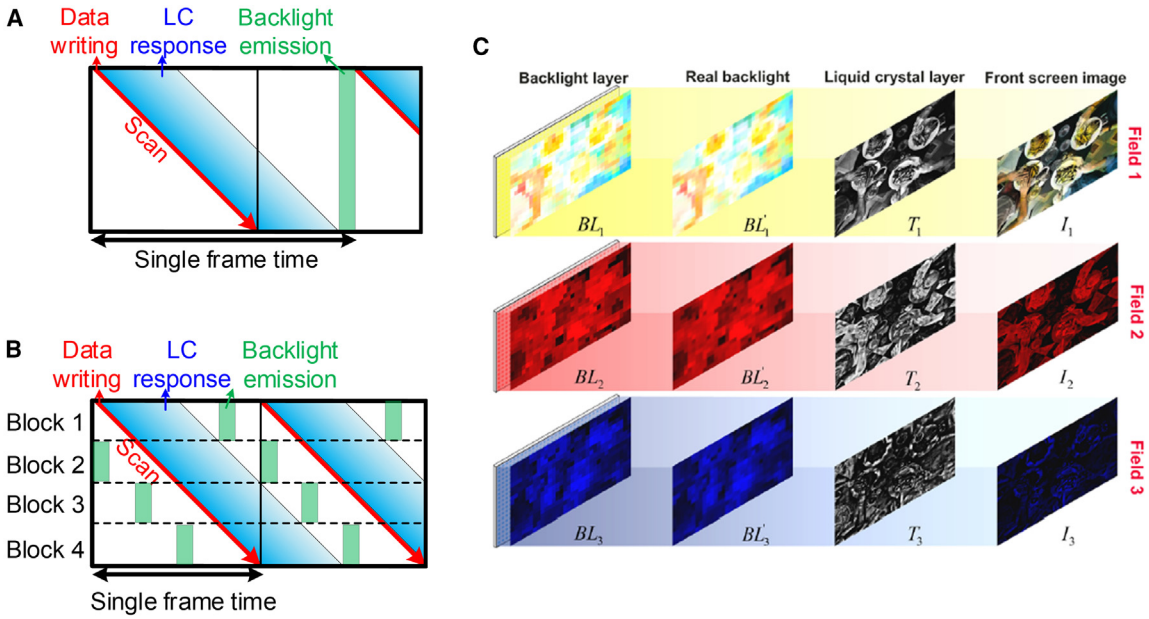

Figure 3. Driving methods and the decomposition algorithm for mitigating the CBU issue

(A) Schematic of simultaneous emission. Backlight is turned on for a short time to suppress motion artifacts.

(B) Schematic of progressive emission in mini-LED backlit AMLCDs. Four blocks are denoted as an illustrative example.

(C) Schematic of the LBGNN-Stencil algorithm. BL_1 is predicted by lightweight backlight generation neural network (LBGNN). Reprint with permission from Wang et al., Opt. Express **31**, 17999–18016 (2023).[30] © The Optical Society.

nickel doping,[24] swelling-deswelling microencapsulation,[25] and multi-amine ligand[26] have been proposed to achieve a more stable PeQD film.

FSC AMLCD

For a color-filter-based AMLCD, it is challenging to achieve a resolution density over 2,000 PPI because of its small aperture ratio. To overcome this hurdle, FSC is a feasible approach. Instead of spatial color mixing, FSC AMLCDs leverage temporal color mixing of several flashing subframe images, as shown in Figure 2B. By eliminating the RGB color filters, FSC AMLCDs can triple the resolution density and optical efficiency. Although FSC AMLCDs have tremendous benefits, the color breakup (CBU) hinders its widespread application. Figure 2C explains the origin of the CBU: when a saccadic eye movement or smooth pursuit of a moving object induces a relative speed between the viewer's eye and the image, the sequentially displayed subframes cannot be perfectly overlapped on the retina, leading to the CBU. When the subframe images move toward the right direction relative to the human eyes, the red fringe and blue fringe will occur in the most left and most right of an image (Figure 2C). The green subframe may mix with the preceding red and succeeding blue subframe to generate intermediate yellow and cyan colors in the left and right side, respectively (Figure 2C).

To quantitatively evaluate the CBU, one may simulate CBU images by shifting each subframe for a certain number of pixels relative to a preceding subframe, and then calculate the difference between CBU images with original images using an average CIEDE2000 color difference. The shift value d in pixels can be calculated by

$$d = \frac{w}{FoV} \cdot \frac{v}{R} \cdot DR \qquad \text{(Equation 4)}$$

where w is the horizontal resolution in pixels, FoV is in degrees, v is the moving speed in degrees per second, R is the subframe (refresh) rate in hertz, and DR is the duty ratio, which is the ratio of the backlight-on time to the frame time. According to Equation 4, a straightforward method of suppressing the CBU is to pursue a higher subframe rate R and thereby reduce the shift value d among the subframes.

A high subframe rate poses great challenges to LC response time. Recently, a fast LC response time of 1.5 ms using a high birefringence material and zero-degree rubbing angle has been demonstrated.[27] Ferroelectric LCs can also exhibit fast response time, but the driving circuits remain to be improved. For example, the number of TFTs should be decreased to boost the aperture ratio. The maximum achievable subframe rate also depends on the driving methods. Figures 3A and 3B show the timing diagram of AMLCDs with simultaneous emission and progressive emission,[28] respectively. In the simultaneous emission, the backlight is turned on following the scanning process and the LC reorientation, as indicated by the green box in Figure 3A. A short backlight-on window helps reduce the motion blur via enabling a low duty ratio, but an instant high current is required to generate the targeted brightness. A larger driving current of the power source may reduce the LED backlight efficiency and worsen the current-resistance effect (I-R drop) on the power source line. Besides, the LC transition and backlight-on window account for a certain portion of frame time and thus limit the frame rate. For the

progressive emission, a mini-LED backlight is required to turn on backlight zones sequentially after the scanning process and the LC reorientation. Because the backlight of each block in Figure 3B is independent, the backlight of the first few blocks can be turned on while the LCs of the last few blocks are still under reorientation. In this way, the frame rate of the display can be higher. Such a progressive emission, together with fast scan time (e.g., 1.7 ms), allows for a ~600-Hz subframe rate. Such a fast scan time can be achieved via writing data for multiple gate lines in different blocks synchronously.[29] It is noted that the sum between a fast LC response time (1.5 ms) and backlight-on time (0.17 ms, corresponding to 10% persistence) is also less than a subframe time to preserve image fidelity. Through a high subframe rate, the CBU can be mitigated because of reduced spatial shift between subframes, but the dynamic electrical power consumption may slightly increase.

In addition to increasing the subframe rate, various decomposition algorithms have been proposed, such as Stencil,[31] LBGNN-Stencil,[30] local primary desaturation (LPD),[32] and Edge Stencil.[33] Conventional RGB FSC display decomposes an image into three subframes where the individual RGB backlight is turned on in the first, second, and third subframe, respectively, as Figure 2C shows. Compared to RGB FSC, the Stencil method adopts a multi-color image as the first subframe. During the first subframe, RGB LEDs are simultaneously turned on to generate high luminance and rough color.[31] In this way, the luminance of the remaining mono-colored subframes is reduced and thus the CBU is suppressed. A multi-color image requires a mini-LED backlight to enable local dimming. The backlight intensities of RGB LEDs are obtained by averaging the RGB components of pixel values in each dimming zone, respectively. Then the LC transmittance can be determined according to diving the pixel value by the backlight intensity. Nevertheless, the image distortion can be noticeable depending on the image contents because of the clipping effect. To obtain the delicate balance between CBU and distortion, Wang et al.[30] adopted the multi-objective genetic algorithm based on the linear weighting and proposed the lightweight backlight generation neural network (LBGNN). Such a neural network was trained by optimization results of the DIV2K database (2,000 resolution images), which could predict a multi-color real-time backlight BL_1 in the first subframe, as shown in Figure 3C. The remaining mono-colored backlight, BL_2 and BL_3, and the LC transmittance can be determined using the same method as Stencil. Therefore, the algorithm is named LBGNN-Stencil.

To preserve the image fidelity while mitigating the CBU, Zhang et al.[32] proposed an LPD backlight driving. Compared with conventional RGB FSC, the backlight colors are not pure RGB; instead, the backlight colors for three subframes are desaturated to reduce the color difference between subframes and suppress perceived CBU. The new three primaries can be determined via searching the minimum triangle that encloses all the chromaticity coordinates of the image in the CIE 1931 *xy* or CIE 1964 *uv* color space. For each of the three subframes, RGB LEDs are lit with a certain intensity ratio to match the chromaticity coordinate of the corresponding new primary. Such a method usually requires a mini-LED backlight because it is more feasible to desaturate the backlight color for a small region of an image instead of the entire image. Nevertheless, the LPD method does not work too well for a very vivid image. Zhang et al. also proposed a hybrid spatial-temporal color display with LPD with two subframes and two color filters.[34] The LPD helps mitigate the CBU, and two temporal fields help reduce the flicker and data transmission bandwidth, but the spatial resolution is just increased by 1.5× rather than 3×.

As mentioned before, Stencil and LPD rely on local dimming to mitigate the CBU well. Inevitably, the cost and burden of hardware and software increase. To suppress CBU using global dimming, Lin et al.[33] proposed an Edge Stencil algorithm that introduces the first mono-colored field to present extracted edge information and used three additional mono-colored (RGB) fields to present remaining information. Since the edge where the CBU probably occurs are mostly concentrated in the first field, the CBU can be suppressed. Compared to Stencil, which adopts the averaged colors in each dimming zone as the backlight color, the Edge Stencil method adopts the averaged edge colors in an entire image as the backlight color in the first subframe. Despite low-cost global dimming, the Edge Stencil method relies on the homogeneity of edge colors and requires four subframes that pose a challenge to the refresh rate. Overall, each method has its pros and cons, and the effectiveness depends on the image contents. LBGNN-Stencil is expected to be less dependent on the image contents, but the computational speed, power consumption, and cost have yet to be fully examined for VR applications. In the following, we introduce a competing light engine called micro-OLEDs that can exhibit both high resolution density and compact formfactor.

MICRO-OLEDs

Conventional OLED display uses a glass substrate with TFTs, which is widely used in smartphone and television displays. However, the requirement of multiple TFTs for each pixel limits the maximum resolution density to ~1,000 PPI. To increase the resolution density, micro-OLEDs have been developed via depositing organic molecule layers (front plane) on top of a silicon CMOS (complementary metal-oxide-semiconductor) backplane instead of glass substrates. Depending on the layer architectures of the front plane, micro-OLED can be categorized into white OLEDs (WOLEDs) with patterned color filters, and patterned RGB OLEDs. WOLEDs are easier to manufacture because their resolution density is determined by color filters that can be fabricated by mature photolithography methods, while RGB OLEDs usually require a fine metal mask (FMM) to define the RGB subpixels. However, it is challenging to fabricate small-pitch (<10-μm) FMMs because of the shadow effect, which originates from the oblique incidence of the depositing particles after passing the metal mask. Overall, micro-OLED can exhibit high resolution density, compact formfactor, and fast response time. Despite their many advantages, their panel size and current efficiency remain to be improved to achieve wide FoV and low-persistence VR displays.

Compared with mature LC materials,[35] OLED materials, especially for blue OLEDs, are still constantly improving. OLED material can be categorized into several types: fluorescence, phosphorescence, thermally activated delayed fluorescence (TADF), and hyperfluorescence. Under applied voltage between

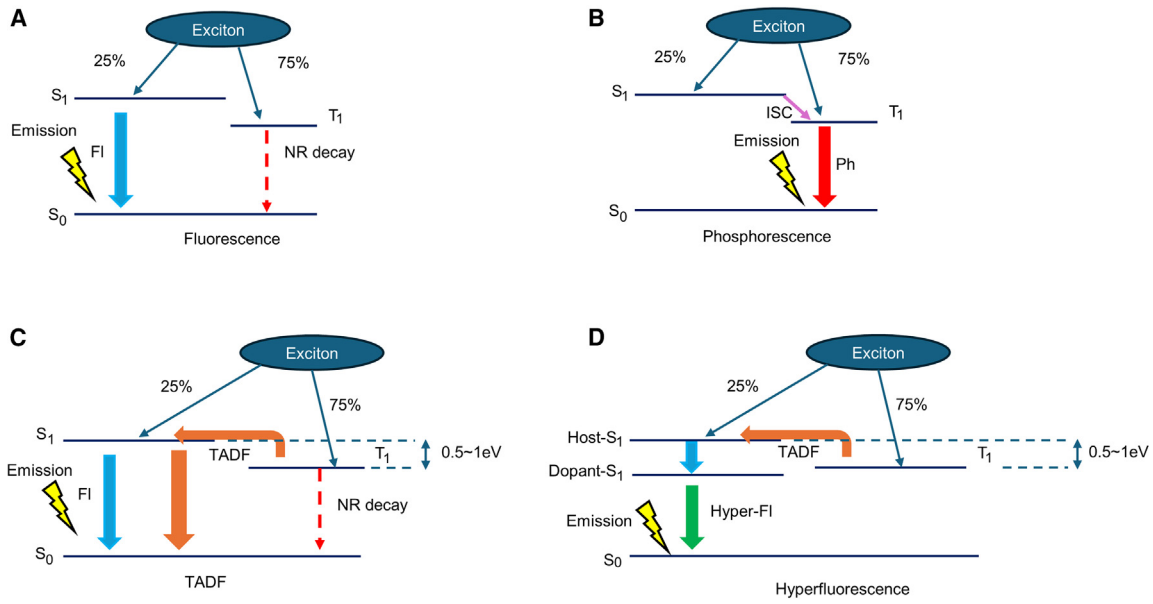

Figure 4. Various OLED emission mechanisms

(A) Fluorescence (denoted by a cyan line).

(B) Phosphorescence (denoted by a red line).

(C) TADF (denoted by an orange line).

(D) Hyperfluorescence (denoted by a green line). Fl, fluorescence; NR decay, nonradiative decay (denoted by a red dashed line); Ph, phosphorescence; ISC, intersystem crossing; Hyper-Fl, hyperfluorescence.

anode and cathode, one electron-hole pair forms an exciton. There are four possible basic states for an exciton: $|0,0\rangle$, $|1,1\rangle$, $|1,0\rangle$, and $|1,-1\rangle$. The spin angular momentum for the $|0,0\rangle$ is 0, which belongs to the singlet state. The spin angular momentum for other cases is 1, which belongs to the triplet state. Therefore, an exciton has 25% or 75% possibilities to be at a singlet state or at a triplet state, respectively. As shown in Figure 4A, traditional fluorescent OLED only utilizes the singlet exciton's light emission so that the maximum internal quantum efficiency (IQE) is limited to 25%. In comparison, phosphorescent OLED can inherently achieve 100% IQE from the intersystem crossing of singlet exciton to triplet state (Figure 4B). Limited by long triplet lifetime and high energy of the excited triplet annihilation, blue phosphorescent materials are facing severe lifetime problems. Recently, Zhao et al. combined blue phosphorescent OLED with plasmon-exciton-polaritons-enhanced Purcell effect and thus enhanced its LT90 (i.e., lifetime when OLED luminance decays to 90% of initial luminance) to 140 ± 20 h.[36] Additionally, continuous efforts are devoted to improving the blue fluorescence OLED. The TADF process is described in Figure 4C. By reducing the exchange energy between the singlet and triplet energy levels, triplets can be converted to singlet by thermal activation, which delays the fluorescence emission and increases the theoretical IQE to 100%. By forbidding nonradiative decay and conveying singlet and triplet exciton energies to final fluorescent emitters through Förster resonance energy transfer, hyperfluorescence OLED materials inherently exhibit a high peak brightness and saturated colors (Figure 4D). Braveenth et al. applied two deep-blue TADF materials to obtain a maximum external quantum efficiency (EQE) of 33.2%.[37] They also achieved a 19-nm FWHM and 38.8% EQE by hyperfluorescence. In addition, Chan et al. demonstrated blue hyperfluorescence OLEDs with 32% EQE at 1,000 cd/m^2, 19-nm FWHM, and LT95 of 18 h based on a two-unit tandem structure.[38]

White micro-OLEDs

Due to its better stability, most of the present commercial WOLED products employ the blue fluorescence emitters and yellow, green, or red phosphorescent emitters, which are named hybrid WOLEDs. Figure 5 shows typical device structures of WOLEDs with different numbers of stacks and colors. The simplest architecture is the single-stack WOLED shown in Figure 5A. It consists of a reflective anode (Al/TiN compatible with the CMOS process), a hole injection layer (HIL), a hole transport layer (HTL), emission layers (EMLs), an electron transport layer (ETL), an electron injection layer (EIL), and a cathode. White light is generated via the combination of a blue EML, a green EML, and a red EML, which Sony demonstrated in 2019.[39] Compared to common single-stack WOLED displays (~2 cd/A), Sony employed an InZnO cathode, a micro-lens array, and optimized color filters to achieve a current efficiency of 6 cd/A and a color gamut of 108% sRGB. Despite its simple architecture, the efficiency and lifetime of the single-stack WOLED microdisplay remain to be improved because only about 25% of the white light transmits through the color filters.

To improve the efficiency and lifetime, tandem WOLEDs[40] have been proposed. They are constructed by two or more EMLs that are connected by charge-generation layers (CGLs). The CGL usually consists of an n-p semiconductor heterojunction layer,[41] responsible for charge generation. The p-CGL and

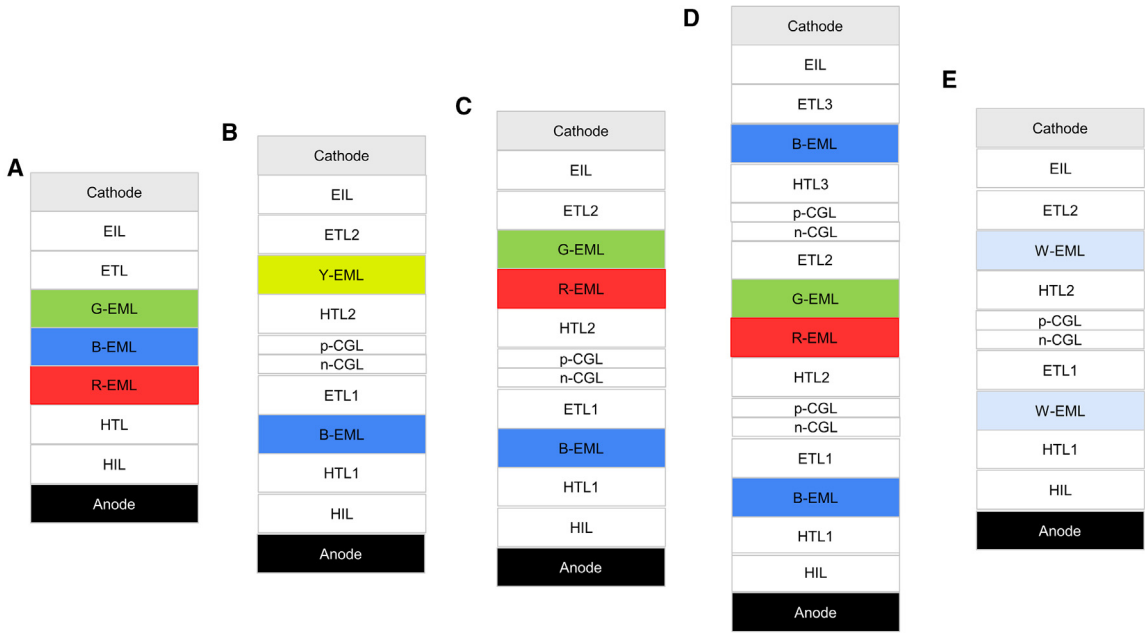

Figure 5. Various types of WOLEDs including tandem structures

(A) One-stack three-color WOLED architecture, in which white light is generated by the combination of three EMLs.

(B) Two-stack two-color tandem WOLED architecture, in which white light is generated by the combination of two EMLs that are connected by a CGL.

(C) Two-stack three-color tandem WOLED architecture, in which white light is generated by the combination of three EMLs that are connected by a CGL.

(D) Three-stack three-color tandem WOLED architecture, in which white light is generated by the combination of four EMLs that are connected by two CGLs.

(E) Two-stack two-white tandem WOLED architecture, in which two white EMLs are connected by a CGL. It is noted that color filters are needed to generate primary colors from WOLEDs.

n-CGL should exhibit low operating voltage, efficient charge generation, high transparency, excellent conductivity, and good thermal stability. Therefore, engineering CGL materials is critical for high-performance tandem WOLEDs.[42] Figures 5B–5E show various architectures of tandem WOLEDs. The two-stack tandem WOLED is shown in Figures 5B and 5C. In comparison with single-stack WOLED, the two-stack WOLED consists of two spatially separated recombination zones by a CGL. By doing so, one electron-hole pair can generate photons twice, doubling the current efficiency. Furthermore, two spatially separated recombination zones enable different EMLs to be placed in the respective antinode positions, where the light wave emitted from the EML is constructively interfered to maximize the light extraction efficiency. The thinnest tandem WOLED device can be obtained via locating all the EMLs at the respective first antinodes, contributing to reducing the driving voltage.[43]

Kopin et al. demonstrated a two-stack WOLED microdisplay with an average current efficiency of 12 cd/A.[44] The more-than-twice improvement arises from material selections and optimal cavity designs. The boosted efficiency enables WOLEDs to achieve a much higher luminance at the same current, or a much longer lifetime at the same luminance. The trade-off of tandem WOLEDs is the increased operating voltage and increased material costs owing to additional CGLs and EMLs. Efficient electron injection and hole injection help lower the operating voltage of tandem WOLEDs. For example, Cho et al. reported a two-stack two-color tandem WOLED with the n-doping ETL and p-doping HIL to lower the operating voltage.[45] To enhance the color performance, one may replace the yellow EML with a red EML and a green EML, as shown in Figures 5C and 5D. The operating voltage may increase because of an additional EML or an additional stack.

To further improve the efficiency of the two-stack tandem WOLED, one may use three stacks consisting of two blue EMLs and a unit including red and green EMLs (Figure 5D). For example, Song et al. demonstrated a three-stack WOLED with wide color gamut and high efficiency,[46] and, in 2024, LG Display also reported a three-stack WOLED to obtain a higher current efficiency than the two-stack WOLED. To generate white emission, one may also use a single EML consisting of a host doped with various color guests,[47] which requires precise doping engineering. Likewise, one may use two white EMLs and a CGL to constitute a two-stack tandem WOLED and thereby to enhance the efficiency, as shown in Figure 5E. It is noted that more stacks (>three stacks) can be connected by CGLs to further improve the efficiency, as demonstrated by OLEDWorks,[48] but the voltage range of the CMOS backplane may pose a constraint on the number of stacks, which is different from television or automotive applications.[49] Overall, a high current efficiency (~54 cd/A) can be obtained via further improving Kopin's two-stack WOLED (12 cd/A) with Sony's methods (~3× increase) and an additional stack (~1.5× increase). Such a high efficiency helps lengthen the lifetime of micro-OLEDs and save power consumption of the VR headset.

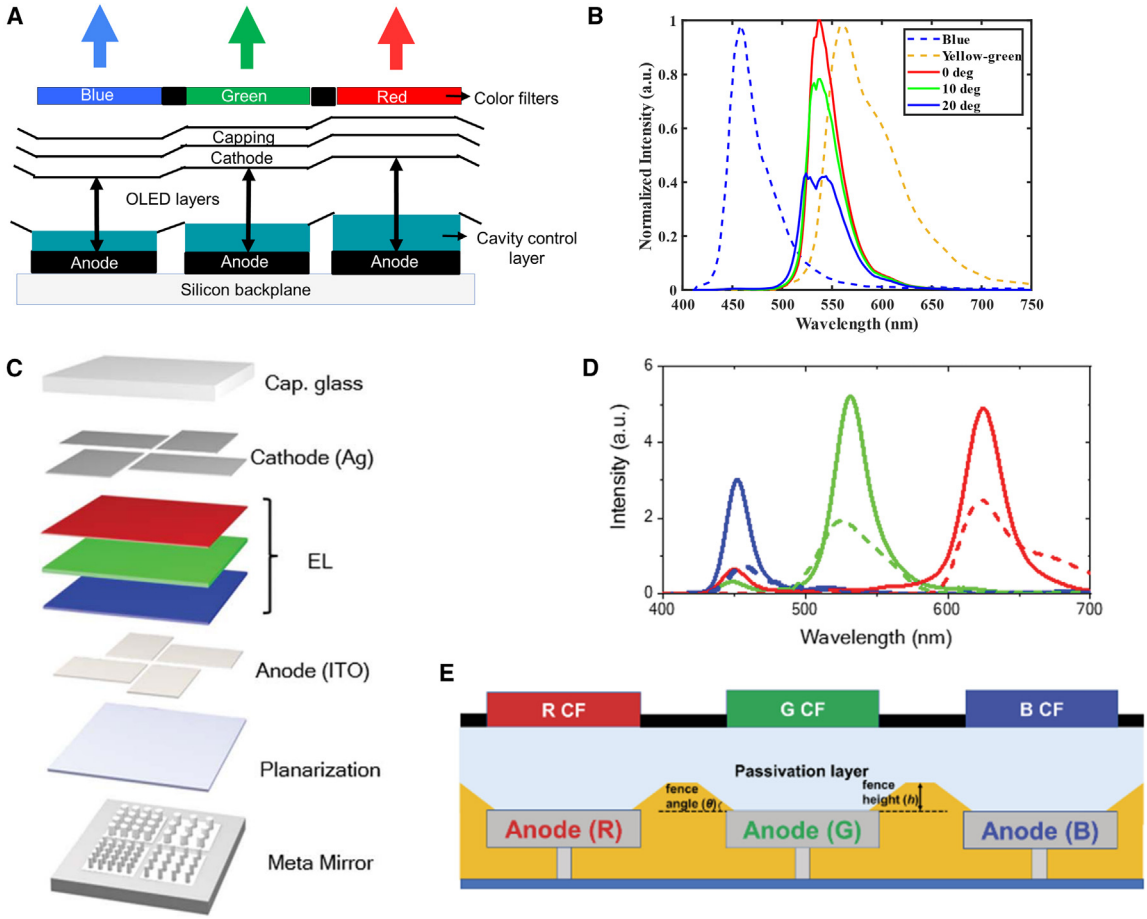

Figure 6. Advanced display architectures of microcavity WOLEDs

(A) Schematic of CCL-based microcavity tandem WOLEDs.

(B) Simulated spectra of the green subpixel in the CCL-based WOLEDs indicated by solid lines. Dashed lines represent the spectra of blue and yellow-green emitters.

(C) Schematic of metasurface-based microcavity WOLEDs (meta-OLEDs). Reprinted by permission from Joo et al., Science **370**, 459–463 (2020).[51] © 2020 AAAS.

(D) Electroluminescent spectra of OLEDs. Solid curves represent the emission from RGB pixels in the metasurface-based WOLED. Dashed curves refer to the emission from RGB pixels in the color filter-based WOLED. Reprinted by permission from Joo et al., Science **370**, 459–463 (2020).[51] © 2020 AAAS.

(E) Schematic of pixel structure with fence between anodes for reducing color crosstalk. Reprinted from Sim et al., Opt. Express **30**, 24155–24165 (2022).[52] © The Optical Society.

In addition to high efficiency, color fidelity is also critical for VR applications. Owing to the wide emission spectra and crosstalk of the employed color filters, the color gamut of WOLEDs is usually smaller than 100% DCI-P3 (e.g., Apple Vision Pro has a color gamut of 92% DCI-P3). To break the color gamut limit, microcavity tandem WOLED with a patterned cavity control layer (CCL)[50] has been demonstrated, as shown in Figure 6A. The patterned CCL can introduce pixelated phase delays corresponding to RGB subpixels. The cathode thickness controls how strong the microcavity effect can be. Leveraging microcavity effects, one may tune the CCL thickness to achieve desired narrow spectra (Figure 6B) before the light transmits through color filters. More specifically, one may locate one EML at an antinode and another EML at a node. Through careful designs of high-order antinodes and nodes, one may achieve a color gamut of 95% Rec. 2020 and 92% Rec. 2020 in the B/G/R WOLED (Figure 5C) with a moderate microcavity effect, and B/Y WOLED (Figure 5B) with a strong microcavity effect, respectively. Blue and green color filters can be removed to further improve the efficiency, but it is hard to remove the red color filters because the undesirable blue sideband in the red subpixel can degrade the color purity. More specifically, the n-order resonant condition for red light resembles $(n + 1)$-order resonant condition for blue light. Recently, Joo et al. proposed a metasurface-driven OLED display,[51] as schematized in Figure 6C. By varying the pillar pitch, one may tune the effective index of the nanopillar medium and thus the effective cavity length. As Figure 6D shows, such a meta-OLED (solid curves) exhibits a narrower emission FWHM and a higher efficiency benefiting from the Purcell effect in the microcavity than the non-cavity WOLEDs with color filters (dashed

curves). It is noted that the undesirable blue sideband from the red subpixel (Figure 6D) can be suppressed via optimized meta-mirror designs.

Another factor related to color performance is the crosstalk between adjacent subpixels in WOLEDs. Although tandem WOLEDs exhibit a much higher current efficiency, a much thicker OLED layer may cause a larger optical crosstalk[53]; a conductive CGL may spread current laterally, aggravating electrical crosstalk.[54] To mitigate the color crosstalk of WOLEDs, Sim et al. investigated various factors such as black matrices, thickness and refractive index of the passivation layer, and fence angle and thickness,[52] as shown in Figure 6E. A thin passivation layer with high refractive index, wide black matrix widths, and high fence angle and height help suppress color crosstalk among subpixels and thus contribute to a wide color gamut. Also, CCL-based microcavity tandem WOLEDs may exhibit less optical crosstalk than microcavity tandem WOLEDs without CCL because the emitted white spectra have been narrowed before it travels through color filters.

RGB micro-OLEDs

Although tandem WOLEDs can exhibit a high current efficiency (luminance per ampere), the operation voltage increases with the number of tandem units so that the power saving may not be significant considering luminance per electrical wattage. As a comparison, RGB OLEDs, which usually require FMMs to define subpixels, can provide at least 4× improvement in operation efficiency by eliminating the color filters. To achieve a high-resolution-density RGB micro-OLED, both FMM thickness and the size of open holes on FMM should be reduced. However, it is challenging to pattern a high-resolution-density FMM over 600 PPI using traditional fabrication methods such as cold rolling and wet etching. For cold-rolling processes, the metal strip is compressed by rollers below its recrystallization temperature. Nevertheless, it is difficult to reduce the FMM thickness below 20 μm due to large surface waviness,[55] resulting in a significant shadow effect during the evaporation. Electroforming masks can achieve an improved hardness,[56] while a large total pitch deviation may induce color-mixing issues. For chemical etching processes, the metal strip is selectively etched using a mask template, while a double-side etching process is required to avoid under-cut.[57] Therefore, the severe shadow effect and reduced quality of the FMM would limit its application in microdisplays.

Among different FMM preparation technologies, laser patterning shows a tremendous advantage in further reducing the pixel size because of the following reasons: short pulse laser avoids overheating induced deformation[55]; FMM thickness can be reduced to below 10 μm because it only requires one-side patterning; and the laser beam size can be controlled below 4 μm. On the other hand, long processing time and nonuniformity are the main challenges for mass production. In 2023, APS Corp. introduced a laser-patterned thin FMM combined with thickness-control process and thereby achieved over 3,000 PPI.[58] Besides laser-assisted FMMs, conventional reactive ion etching-coupled photolithography is capable of fabricating sub-micro-scale patterns. In 2022, Kweon et al. demonstrated 4,500 PPI multi-color OLED panel,[59] while the fabrication difficulty, reduced material quality, and increased driving voltage limit its further development. Japan Display developed lithography with maskless deposition to pattern RGB subpixels more precisely, which increases the aperture ratio to 60%.[60] In 2022, Semiconductor Energy Laboratory (SEL) also demonstrated a 1.50-inch 3,207-PPI RGB micro-OLED panel with an aperture ratio of 53.7%.[61] Maskless lithography remains to be examined for its mass production feasibility. As another kind of manufacturing technology, electrohydrodynamic jet printing can achieve a 5-μm pixel size by pulling liquids out of the metal-coated nozzle through the electric field generated from the nozzle and the conductive substrate.[62] To enable its application in microdisplays, the issues of low printing uniformity, demanding OLED materials, and high applied voltage between the nozzle and substrate should be addressed.[63] Overall, RGB micro-OLEDs require further development in cost-effective manufacturing.

Like tandem WOLEDs, a tandem structure also applies to RGB OLEDs to improve the current efficiency, as schematized in Figure 7A. The EMLs of two stacks can be placed at corresponding (e.g., the first and the second) antinodes (as denoted by dotted lines in Figure 7A) to maximize the light-extraction efficiency (LEE). Nevertheless, the total internal reflection at the interfaces between high-index organic materials, glass, and air limits further LEE improvement. To boost the LEE of tandem RGB OLEDs, one may concentrate more light energy onto the air mode through the microcavity effect,[64] resulting in directional emission. To resonate with RGB wavelengths, different cavity lengths are required in RGB OLEDs, as indicated by Figure 7A. Figure 7B shows that, as the number of stacks increases, the waveguide modes become more dominant.[65] Consequently, additional light extraction structures are necessary to extract the waveguide modes into the air mode and improve the LEE. Common methods include using scattering/diffraction or patterned interfaces to redirect light toward the normal direction. Commonly used optical structures include corrugated substrates[66–68] (Figure 7C), embedded scattering layers,[69,70] and micro-lens arrays (Figure 7D).

The light-extraction process is closely tied to the directionality of emitted light. While the above-mentioned methods are commonly employed to enhance the LEE of OLEDs, their application to VR displays necessitates careful consideration of emission directionality. In VR displays, a relatively small emission cone ($\pm 20^{o}$) is crucial to form a decent eyebox.[4] Thus, when choosing a strategy to improve LEE, a delicate balance between emission directionality and light-extraction process is essential. As pancake lens is widely used in viewing optics, the polarization of emitted light is also a crucial factor to improve the effective LEE. Instead of using absorptive or reflective polarizers, a polarized OLED could be achieved by maximizing the ratio of the fundamental transverse electric waveguide mode TE_0 and coupling it out with one-dimensional corrugated gratings[66,68] (Figure 7C). However, this method imposes a strict requirement in thin thickness, which is difficult to apply to tandem OLEDs. If an ultrathin Cu-Ag film is employed to replace conventional indium tin oxide (ITO) or Ag,[71] the cutoff thickness for TE_0 will increase. Therefore, the method of generating a polarized OLED still applies to tandem OLEDs.

To summarize, tandem RGB micro-OLEDs can exhibit a higher current efficiency and a wider color gamut than tandem white

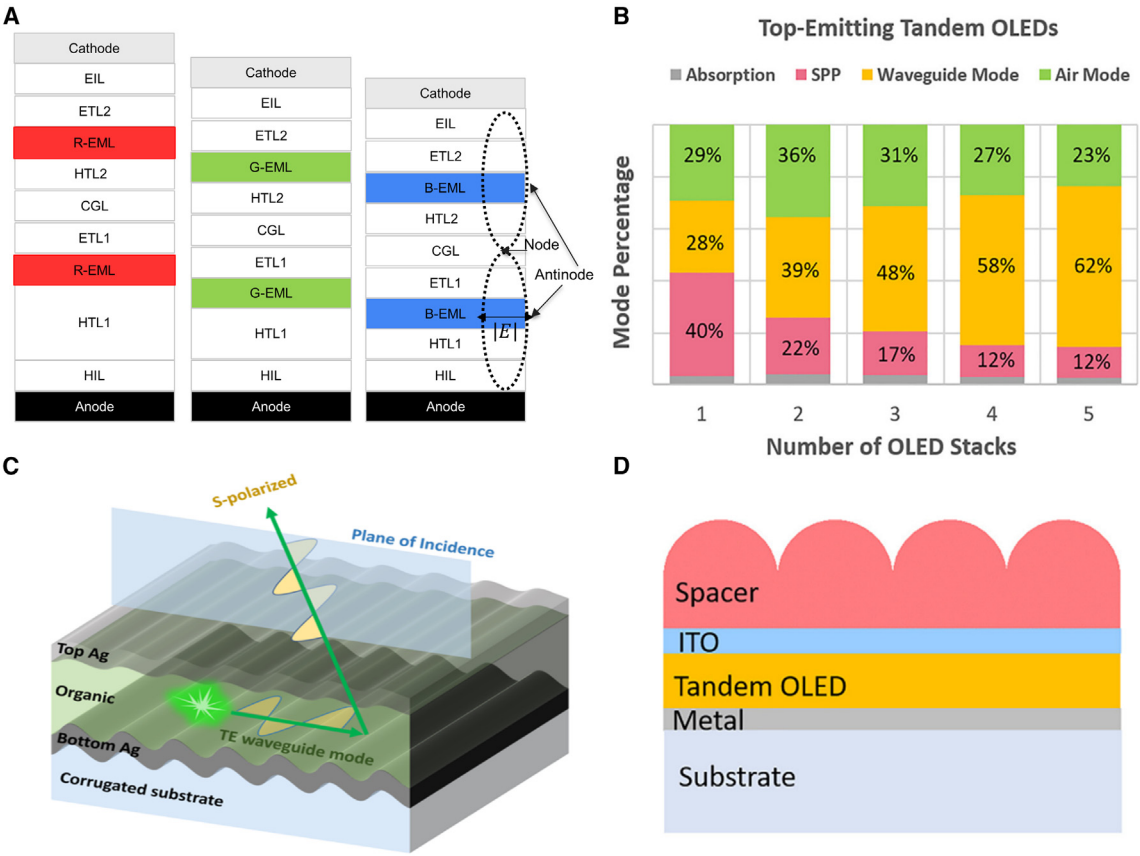

Figure 7. High-performance RGB OLEDs including tandem structures

(A) Schematic of microcavity tandem RGB OLEDs. Dotted lines represent the distribution of the electric-field amplitude in the OLED device corresponding to a blue subpixel.

(B) Calculated mode percentage of a multi-stack top-emitting OLED. Reprinted with permission from Fu et al. Appl. Phys. Lett. **119**, 060504 (2021).[65] © 2021 The American Institute of Physics.

(C) Schematic of a "single-mode" OLED on a corrugated substrate. Reprinted with permission from Dong et al., ACS Photonics **10**, 3342–3349 (2023).[66] © 2023 American Chemical Society.

(D) Schematic of a micro-lens array on tandem OLEDs. Reprinted with permission from Fu et al. Appl. Phys. Lett. **119**, 060504 (2021).[65] © 2021 The American Institute of Physics.

micro-OLEDs via eliminating color filters. However, the maximal resolution density of white micro-OLEDs is presently higher than that of RGB micro-OLEDs because of its simpler manufacturing method. To increase the color gamut of tandem white micro-OLEDs, microcavity with a patterned CCL can be introduced to narrow the emitted spectra of OLED layers before the light passes through the color filters. However, the increased layer thickness would inevitably worsen the color crosstalk. Although the tandem structure improves the current efficiency, its operation voltage increases with the number of tandem units, thus compromising the power saving. To achieve optimized performance of the tandem structures, one should consider the balance between current efficiency, driving voltage, and color crosstalk.

VIEWING OPTICS

For a VR display system to function, an imaging optics is placed between the display panel and the user's eye to magnify the image. In this section, we focus on the formfactor, efficiency, and stray-light problem related to the optics system design.

Fundamental architectures

A basic VR system includes a display as the light source and a refractive lens for imaging purpose as shown in Figure 8A. However, the formfactor and weight of the headset are often at odds with imaging quality and the FoV. With about 12-mm ER, the large formfactor results from the thickness of the refractive lens itself and its about 4-cm focal length. The working distance between the display and optics is approximately equal to the focal length, forming a magnified virtual image in the distance. Fresnel lenses with a thinner thickness have been employed in Meta Quest 2 to reduce the formfactor. Unfortunately, the distance between the display and optics does not change significantly and most of the volume is still empty, as illustrated in Figure 8B. To reduce the empty space, a hybrid-lenses group depicted in Figure 8C has been proposed and demonstrated.

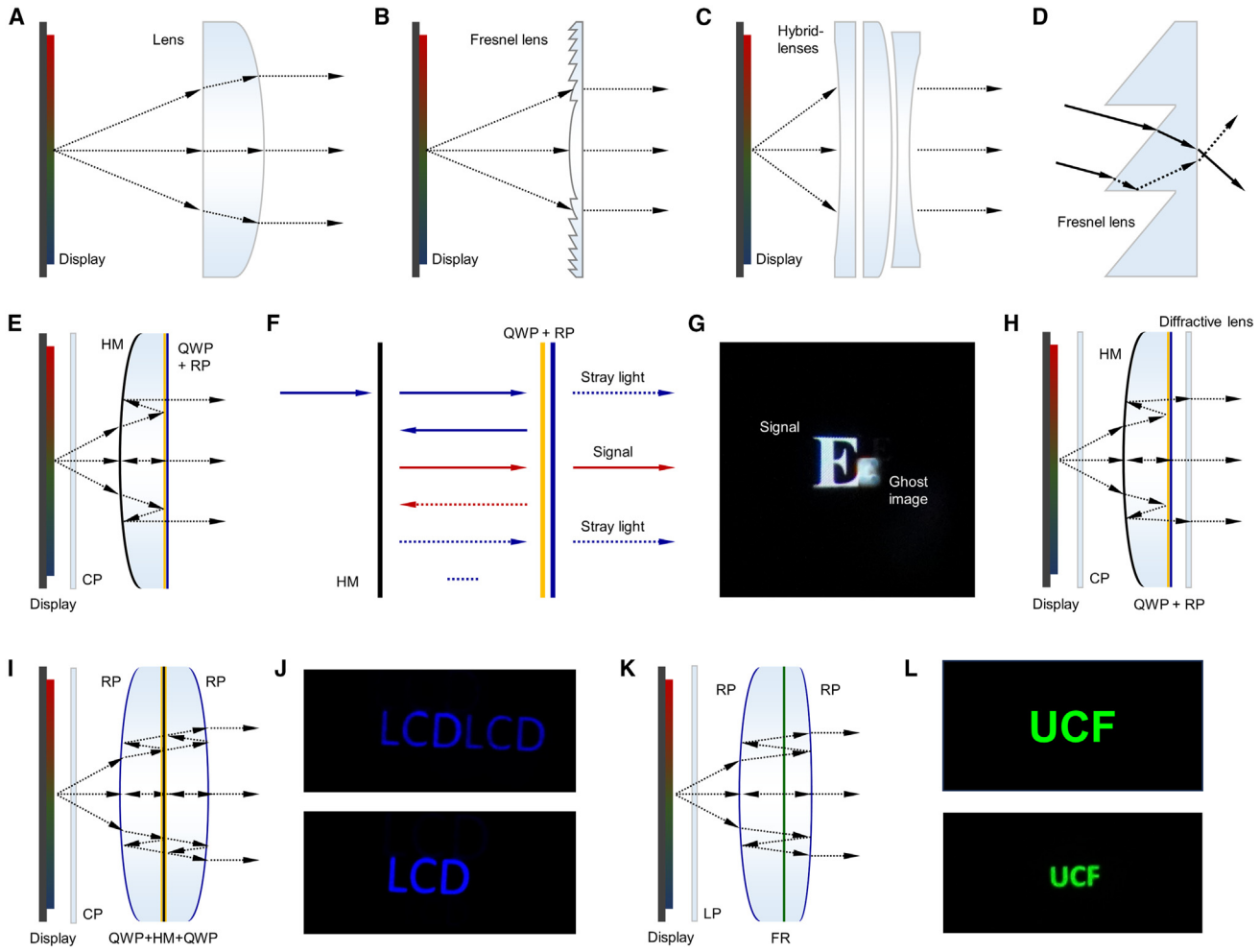

Figure 8. Optical configurations of VR/MR display systems

(A) A basic VR system.

(B) A Fresnel lens as the imaging optics.

(C) Hybrid lenses for VR imaging.

(D) Stray light in a Fresnel lens.

(E) A pancake VR system.

(F) Light paths inside a pancake system.

(G) Ghost image in a VR system.

(H) A VR lens with an additional diffractive lens for better imaging quality.

(I) A double-path pancake system.

(J) Misaligned (top) and aligned (bottom) folded images in the double-path pancake system. Reprinted with permission from Ding et al., Proc. SPIE **12913**, 1291309 (2024).[72] © 2024 SPIE.

(K) A theoretically lossless pancake system with a Faraday rotator (FR).

(L) Original (top) and folded (bottom) images in the FR pancake system. Reprinted with permission from Ding et al., Opto-Electron. Adv. **7**, 230178 (2024).[73]

The system consists of three elements, including aspherical and Fresnel lenses. With an ultra-light weight of 13 g, the total thickness of the lens group is compressed to 21.85 mm while offering a 100° FoV. Such a hybrid-lenses system without folded structure can achieve over 60% light efficiency. However, stray light resulting from Fresnel grooves degrades the system imaging quality, which further affects the immersive visual experience, as Figure 8D depicts.

Providing ultracompact formfactor and excellent imaging quality, a polarization-based folded catadioptric optics (commonly called pancake optics) has become the first choice of present VR and MR headsets, including Meta Quest 3, Quest Pro, Pico 4, and Apple Vision Pro. The system configuration is illustrated in Figure 8E. The emitted light from the display panel is converted to a circularly polarized light by a circular polarizer (CP). For simplicity without losing generality, let us assume the light after the CP is right-handed circular polarization (RCP), which is represented by the solid blue arrows in Figure 8F. The light is incident on a half mirror (HM) and only 50% of the light will keep the same polarization state and pass through the HM.

Table 1. Advantages and disadvantages of different viewing optics

	Formfactor[a]	Efficiency	Stray light	Manufacture
Refractive lens	large	high	excellent	easy
Fresnel lens	large	high	poor	easy
Hybrid-lenses	large	~60%	poor	easy
Pancake lens	medium[b]	~25%	acceptable	easy
Pancake lens combined with diffractive lens	small	~15%	acceptable	moderate
Double-path pancake lens	medium	~50%	acceptable	easy
Lossless pancake lens	small	~100%	acceptable	difficult

[a]The distance between the display panel and viewing optics has been considered when discussing the formfactor here. For example, the thickness of the Fresnel lens itself is thin but its focal length is much longer compared to the pancake lenses. Therefore, the system formfactor is large, as shown here.

[b]Multiple refractive lenses are integrated in the compound pancake lens of current commercial products such as Meta Quest 3 and Apple Vision Pro, which increase the formfactor.

Half of the light is reflected and wasted with the opposite circular polarization. The remaining light in the forward direction will then be converted to linear polarization by a quarter-wave plate (QWP) and reflected backward after impinging on the reflective polarizer (RP). At the second incidence to the HM surface, only 25% of the total light will be reflected to the QWP and RP with an opposite left-handed circular polarization (LCP) represented by solid red arrows. Finally, the folded light is now able to transmit through the optics and reach the user's eye. The main optical power in such a pancake lens system is provided by the reflection at the curved HM surface, which exhibits a better field curvature performance than conventional refractive lens systems. Therefore, such a pancake lens provides a much larger optical power with the same lens curvature, which further reduces the formfactor of the VR system. Moreover, the reflective surface will not generate chromatic aberrations, which helps minimize color dispersion.

Although the pancake systems offer advantages to formfactor and imaging quality, they suffer from low light efficiency and stray light, which degrades the signal-to-noise ratio. The system efficiency of the pancake lens is limited to 25% for a polarized-light engine and 12.5% for an unpolarized microdisplay due to the existence of the HM. Such a low light efficiency increases the power consumption and reduces the operating time for the battery-powered devices. Besides, the undesired reflections at multiple interfaces, the imperfect polarization conversion, and light leakage from the polarizing components result in stray lights that lower the system contrast ratio.[74–77] Adding anti-reflection coatings helps to reduce the stray light caused by reflections. However, the light leakage and undesired reflections from the RP cause stray lights, which in turn generate more noticeable ghost images as represented by the dashed arrows in Figure 8F. Figure 8G shows the signal and ghost images in a pancake lens. Due to off-axis light leakage of the QWP, the RP magnifies the polarization impurity, which makes it harder to absorb the stray light using a linear polarizer after the pancake lens. One approach is to replace the combination of QWP and RP with a cholesteric LC (CLC) film,[78] which allows high transmission for one circular polarization and high reflection for the opposite component. The pancake system with a CLC film eliminates the alignment issue between the QWP and the RP and provides the possibility to correct the chromatic aberrations as the CLC film can be fabricated with specifically designed phase profile. To enable more degrees of freedom, extra refractive lenses have been combined with the single pancake lens for better imaging performances in current VR and MR headsets. However, more refractive lenses also impose new issues for the formfactor and weight. Diffractive lenses including metalenses[79] and LC flat lenses[80,81] with an ultrathin profile might be good candidates for replacing the additional refractive lenses to alleviate the burden on formfactor and weight, as shown in Figure 8H.

Strategies for higher light efficiency and smaller formfactor

To enhance the light efficiency, several optical configurations inspired by the pancake system have been proposed. The first one, called the double-path pancake system,[82,83] shows a symmetrical configuration, as illustrated in Figure 8I. In addition to the components in a traditional pancake system, the double-path system recycles the wasted light by adding a mirrored QWP and RP between the CP and the HM. The 50% wasted light in the original system will now be reflected to the HM by the new polarizing elements, which doubles the system light efficiency from 25% to 50% for a polarized input, as depicted in Figure 8J.[72] Besides, the two pairs of QWPs and RPs could be replaced with a CLC reflector to form a similar double-path pancake system.[83] Although the optical efficiency gets improved, the lens design between these two RPs or CLC reflectors is required to be symmetric about the half mirror, which induces a strict alignment requirement, limiting the design freedom and further increasing the volume of pancake lens. Moreover, the inclusion of additional polarizing components may further complicate the polarization issue and degrade the image contrast ratio.

To eliminate the fundamental optical loss caused by the HM and maintain a high design freedom of conventional pancake optics, a lossless pancake optics was proposed.[73] Such a novel pancake optics includes a nonreciprocal polarization rotator (e.g., Faraday rotator) sandwiched between two RPs, as shown in Figure 8K. Compared to a reciprocal polarization rotator (e.g., half-wave plate), the nonreciprocal polarization (Faraday) rotator

is directly proportional to the magnetic field and the rotation direction (θ(λ)?) is solely determined by the magnetic field, irrespective of the optical wave's propagation direction, as follows:

$$\theta(\lambda) = V(\lambda)BL, \quad \text{(Equation 5)}$$

where $V(\lambda)$ denotes the Verdet constant of the material, B represents the magnetic flux density in the propagation direction, and L stands for the length of the magneto-optical element. By utilizing this property, the light path can be folded three times without losing energy (Figure 8L). Besides, the novel pancake optics system retains a high design freedom because it does not require symmetric design. However, to truly achieve a compact formfactor, a thin-film Faraday rotator is required. This further requires the development of magneto-optic materials. First, the magneto-optic materials with a large Verdet constant and low absorption in the visible region are required to make a thin-film Faraday rotator. Second, unlike some commercial magneto-optic materials that require an external magnet or solenoids, the Faraday rotator must be magnet-free (e.g., bismuth substituted rare-earth iron garnets).[84] The advantages and disadvantages of viewing optics are summarized in Table 1.

CONCLUSIONS AND OUTLOOK

We have reviewed emerging approaches that are key enablers for next-generation VR/MR devices. By combining progressive emission, fast scan time, and fast LC response time, one may achieve a high refresh rate (~600 Hz) to mitigate the CBU in FSC AMLCDs. Combining mini-LEDs with AMLCDs will not only save power consumption but also contribute to achieving LBGNN-Stencil or LPD to suppress the color breakup. Such an FSC AMLCD with reduced CBU is expected to stand out in next-generation high-resolution-density VR displays with a low cost. In parallel to advancing FSC AMLCDs, tandem white micro-OLEDs and tandem RGB micro-OLEDs are actively investigated to improve the efficiency and color gamut in terms of materials, optical structures, and manufacturing. In the near term, microcavity tandem white micro-OLED with two (or three) stacks, CCL, and micro-lens array may prevail in high-end VR displays because of its improved current efficiency and expanded color gamut. In the long term, as manufacturing methods become more mature, microcavity tandem RGB micro-OLEDs exhibit an enormous potential to compete with white micro-OLEDs because of their much higher (~4×) light efficiency.

As for viewing optics, pancake lens has now become the mainstream of commercial products due to its compact formfactor and good image quality. A compound pancake lens usually consists of several refractive lenses for better imaging quality, where achromatic diffractive optics can be used to further reduce the formfactor. However, the low optical efficiency originating from the half mirror in the folded system remains to be overcome. Some approaches have been demonstrated to enhance the pancake system efficiency to 50% (using the double-path pancake lens) or even 100% (using the Faraday rotator pancake system). The double-path pancake lens can be fabricated easily with current technology, while the lossless pancake system calls for a thin-film nonreciprocal polarization rotator to be developed. These high-efficiency and compact viewing optics are anticipated to elevate the next-generation VR systems with a longer wearing time and more comfortable user experience.

ACKNOWLEDGMENTS

This work was partially supported by Goertek Electronics and The University of Central Florida Board of Trustees.

AUTHOR CONTRIBUTIONS

Z.Y. initiated the project. Z.Y., Z.L., Y.D., Y.Q., and S.-C.C. conducted the simulation and wrote the manuscript. C.-L.L. and S.-T.W. supervised the project and edited the manuscript.

DECLARATION OF INTERESTS

The authors declare no competing interests.

REFERENCES

1. Ding, Y., Yang, Q., Li, Y., Yang, Z., Wang, Z., Liang, H., and Wu, S.-T. (2023). Waveguide-based augmented reality displays: perspectives and challenges. eLight *3*, 24. https://doi.org/10.1186/s43593-023-00057-z.
2. Maimone, A., and Wang, J. (2020). Holographic optics for thin and lightweight virtual reality. ACM Trans. Graph. *39*, 67. https://doi.org/10.1145/3386569.3392416.
3. Yin, K., Hsiang, E.-L., Zou, J., Li, Y., Yang, Z., Yang, Q., Lai, P.-C., Lin, C.-L., and Wu, S.-T. (2022). Advanced liquid crystal devices for augmented reality and virtual reality displays: principles and applications. Light Sci. Appl. *11*, 161. https://doi.org/10.1038/s41377-022-00851-3.
4. Hsiang, E.-L., Yang, Z., Yang, Q., Lai, P.-C., Lin, C.-L., and Wu, S.-T. (2022). AR/VR light engines: perspectives and challenges. Adv. Opt. Photonics *14*, 783–861. https://doi.org/10.1364/AOP.468066.
5. Hofmann, S., Thomschke, M., Lüssem, B., and Leo, K. (2011). Top-emitting organic light-emitting diodes. Opt Express *19*, A1250–A1264. https://doi.org/10.1364/OE.19.0A1250.
6. Wu, Y.-H., Tsai, C.-H., Wu, Y.-H., Cherng, Y.-S., Tai, M.-J., Huang, P., Yao, I.-A., and Yang, C.-L. (2023). 5-2: Invited Paper: High dynamic range 2117-ppi LCD for VR displays. SID Symp. Dig. Tech. Pap. *54*, 36–39. https://doi.org/10.1002/sdtp.16481.
7. Wu, Y.-H., Chang, C.-C., Tsou, Y.-S., Lo, Y.-C., Tsai, C.-H., Lu, C.h., Yang, C.-L., and Chuang, F.-M. (2023). Enhancing virtual reality with high-resolution light field liquid crystal display technology. J. Opt. Microsyst. *3*, 041202. https://doi.org/10.1117/1.JOM.3.4.041202.
8. Yang, Z., Hsiang, E.L., Qian, Y., and Wu, S.T. (2022). Performance comparison between mini-LED backlit LCD and OLED display for 15.6-inch notebook computers. Appl. Sci. *12*, 1239. https://doi.org/10.3390/app12031239.
9. Lin, C.-C., Wu, Y.-R., Kuo, H.-C., Wong, M.S., DenBaars, S.P., Nakamura, S., Pandey, A., Mi, Z., Tian, P., Ohkawa, K., et al. (2023). The micro-LED roadmap: status quo and prospects. J. Phys. Photonics *5*, 042502. https://doi.org/10.1088/2515-7647/acf972.
10. Hsiang, E.-L., Yang, Z., and Wu, S.-T. (2023). Optimizing microdisplay requirements for pancake VR applications. J. Soc. Inf. Disp. *31*, 264–273. https://doi.org/10.1002/jsid.1199.
11. Kim, J., Billah, M.M., and Jang, J. (2022). Ultra-Low Power, Emission Gate Driver With Pulse Width Modulation Using Low-Temperature Poly-Si Oxide Thin-Film Transistors. IEEE Electron. Device Lett. *43*, 236–239. https://doi.org/10.1109/LED.2021.3137195.

12. Yang, Y., Chen, Y., Xiong, H., Cao, H., Liu, F., Zha, G., and Yuan, J. (2023). 87-5: AM Mini-LED Based on LTPS TFT Backplane with over 5000 Dimming Zones and High Driving Bits. SID Symp. Dig. Tech. Pap. *54*, 1238–1241. https://doi.org/10.1002/sdtp.16802.

13. Kim, J., Chen, Y., Lee, S., and Jang, J. (2021). A Novel Gate Driver Working Under Depletion Mode Oxide TFTs Using Low-Temperature Poly-Si Oxide TFTs. IEEE Electron. Device Lett. *42*, 1619–1622. https://doi.org/10.1109/LED.2021.3110272.

14. Luo, C., Yin, G., Shu, Z., Liu, G., and Ai, F. (2021). P-2: High-Performance LTPO TFT-LCD Using Metal as Hydrogen Barrier Layer. SID Symp. Dig. Tech. Pap. *52*, 1063–1066. https://doi.org/10.1002/sdtp.14875.

15. Jeong, D.Y., Billah, M.M., Siddik, A.B., Han, B., Chang, Y., and Jang, J. (2021). High Performance Dual Gate Blue Laser Annealed Poly-Si Thin-Film Transistor for High-Resolution Displays. IEEE Trans. Electron. Dev. *68*, 3863–3869. https://doi.org/10.1109/TED.2021.3091965.

16. Chen, J.-J., Chang, T.-C., Chen, H.-C., Zhou, K.-J., Kuo, C.-W., Wu, W.-C., Li, H.-C., Tai, M.-C., Tu, Y.-F., Tsai, Y.-L., et al. (2020). Enhancing Hot-Carrier Reliability of Dual-Gate Low-Temperature Polysilicon TFTs by Increasing Lightly Doped Drain Length. IEEE Electron. Device Lett. *41*, 1524–1527. https://doi.org/10.1109/LED.2020.3018196.

17. Lin, C.-L., Chen, F.-H., Wang, M.-X., Lai, P.-C., and Tseng, C.-H. (2017). Gate Driver Based on a-Si:H Thin-Film Transistors With Two-Step-Bootstrapping Structure for High-Resolution and High-Frame-Rate Displays. IEEE Trans. Electron. Dev. *64*, 3494–3497. https://doi.org/10.1109/TED.2017.2710180.

18. Liu, P.-T., Zheng, G.-T., and Lin, Y.-C. (2019). Multioutputs single-stage gate driver on array with wide temperature operable thin-film-transistor liquid-crystal display for high resolution application. J. Soc. Inf. Disp. *27*, 21–33. https://doi.org/10.1002/jsid.742.

19. Lin, C.-L., Deng, M.-Y., Chiu, W.-C., Shih, L.-W., Chang, J.-H., Lin, Y.-S., and Lee, C.-E. (2020). A Pre-Bootstrapping Method for Use in Gate Driver Circuits to Improve the Scan Pulse Delay of High-Resolution TFT-LCD Systems. IEEE Trans. Ind. Electron. *67*, 7015–7024. https://doi.org/10.1109/TIE.2019.2940000.

20. Murphy, J., Camardello, S., Doherty, M., Liu, J., Smigelski, P., and Setlur, A. (2021). 11.1: Invited Paper: Narrow-Band Phosphors for Next Generation MiniLED and MicroLED Displays. SID Symp. Dig. Tech. Pap. *52*, 165–168. https://doi.org/10.1002/sdtp.15052.

21. Wu, Y., Ma, J., Su, P., Zhang, L., and Xia, B. (2020). Full-Color Realization of Micro-LED Displays. Nanomaterials *10*, 2482. https://doi.org/10.3390/nano10122482.

22. Chen, J., Zhao, Q., Yu, B., and Lemmer, U. (2024). A Review on Quantum Dot-Based Color Conversion Layers for Mini/Micro-LED Displays: Packaging, Light Management, and Pixelation. Adv. Opt. Mater. *12*, 2300873. https://doi.org/10.1002/adom.202300873.

23. Li, F., Ji, H., Xu, H., Bai, Z., Liu, R., Li, J., and Zhong, H. (2020). 16-4: Late-News Paper: High Color Gamut Mini-LED Backlight Demon based on Dual-Emissive Perovskite Quantum Dots Films. SID Symp. Dig. Tech. Pap. *51*, 219–221. https://doi.org/10.1002/sdtp.13842.

24. Kim, H., Bae, S.-R., Lee, T.H., Lee, H., Kang, H., Park, S., Jang, H.W., and Kim, S.Y. (2021). Enhanced Optical Properties and Stability of CsPbBr3 Nanocrystals Through Nickel Doping. Adv. Funct. Mater. *31*, 2102770. https://doi.org/10.1002/adfm.202102770.

25. Wang, Y., He, J., Chen, H., Chen, J., Zhu, R., Ma, P., Towers, A., Lin, Y., Gesquiere, A.J., Wu, S.-T., and Dong, Y. (2016). Ultrastable, Highly Luminescent Organic–Inorganic Perovskite–Polymer Composite Films. Adv. Mater. *28*, 10710–10717. https://doi.org/10.1002/adma.201603964.

26. Zeng, Q., Zhang, X., Bing, Q., Xiong, Y., Yang, F., Liu, H., Liu, J.y., Zhang, H., Zheng, W., Rogach, A.L., and Yang, B. (2022). Surface Stabilization of Colloidal Perovskite Nanocrystals via Multi-amine Chelating Ligands. ACS Energy Lett. *7*, 1963–1970. https://doi.org/10.1021/acsenergylett.2c00786.

27. Yang, Z., Qian, Y., Zou, J., Lee, C.-L., Lin, C.-L., and Wu, S.-T. (2023). Reducing the Power Consumption of VR Displays with a Field Sequential Color LCD. Appl. Sci. *13*, 2635. https://doi.org/10.3390/app13042635.

28. Hong, Y.-H., Jung, E.K., Jeong, Y.-R., Im, H., and Kim, Y.-S. (2023). Micro Light-Emitting Diode Pixel Circuit Based on p-Type Low-Temperature Polycrystalline Silicon Thin-Film Transistor for Mobile Displays. IEEE Trans. Electron. Dev. *70*, 4662–4668. https://doi.org/10.1109/TED.2023.3296068.

29. Yamada, F., Nakamura, H., Sakaguchi, Y., and Taira, Y. (2002). Sequential-color LCD based on OCB with an LED backlight. J. Soc. Inf. Disp. *10*, 81–85. https://doi.org/10.1889/1.1827848.

30. Wang, Z., Zou, G., Shen, Y., Yang, B.-R., and Qin, Z. (2023). Deep learning-based real-time driving for 3-field sequential color displays with low color breakup and high fidelity. Opt Express *31*, 17999–18016. https://doi.org/10.1364/OE.487198.

31. Lin, F.-C., Huang, Y.-P., Wei, C.-M., and Shieh, H.-P.D. (2009). Color-breakup suppression and low-power consumption by using the Stencil-FSC method in field-sequential LCDs. J. Soc. Inf. Disp. *17*, 221–228. https://doi.org/10.1889/JSID17.3.221.

32. Zhang, Y., Lin, F.-C., and Langendijk, E.H.A. (2011). A field-sequential-color display with a local-primary-desaturation backlight scheme. J. Soc. Inf. Disp. *19*, 258–264. https://doi.org/10.1889/JSID19.3.258.

33. Lin, F.-C., Qin, Z., Teng, K.-T., and Huang, Y.-P. (2019). Color breakup suppression based on global dimming for field sequential color displays using edge information in images. Opt Express *27*, 2335–2343. https://doi.org/10.1364/OE.27.002335.

34. Zhang, Y., Langendijk, E.H.A., Hammer, M., and Lin, F.-C. (2011). A Hybrid Spatial-Temporal Color Display With Local-Primary-Desaturation Backlight Scheme. J. Disp. Technol. *7*, 665–673. https://doi.org/10.1109/JDT.2011.2159774.

35. Zou, J., Yang, Z., Mao, C., and Wu, S.-T. (2021). Fast-Response Liquid Crystals for 6G Optical Communications. Crystals *11*, 797. https://doi.org/10.3390/cryst11070797.

36. Zhao, H., Arneson, C.E., Fan, D., and Forrest, S.R. (2024). Stable blue phosphorescent organic LEDs that use polariton-enhanced Purcell effects. Nature *626*, 300–305. https://doi.org/10.1038/s41586-023-06976-8.

37. Braveenth, R., Lee, H., Park, J.D., Yang, K.J., Hwang, S.J., Naveen, K.R., Lampande, R., and Kwon, J.H. (2021). Achieving Narrow FWHM and High EQE Over 38% in Blue OLEDs Using Rigid Heteroatom-Based Deep Blue TADF Sensitized Host. Adv. Funct. Mater. *31*, 2105805. https://doi.org/10.1002/adfm.202105805.

38. Chan, C.-Y., Tanaka, M., Lee, Y.-T., Wong, Y.-W., Nakanotani, H., Hatakeyama, T., and Adachi, C. (2021). Stable pure-blue hyperfluorescence organic light-emitting diodes with high-efficiency and narrow emission. Nat. Photonics *15*, 203–207. https://doi.org/10.1038/s41566-020-00745-z.

39. Motoyama, Y., Sugiyama, K., Tanaka, H., Tsuchioka, H., Matsusaki, K., and Fukumoto, H. (2019). High-efficiency OLED microdisplay with microlens array. J. Soc. Inf. Disp. *27*, 354–360. https://doi.org/10.1002/jsid.784.

40. Xiao, P., Huang, J., Yu, Y., and Liu, B. (2019). Recent Developments in Tandem White Organic Light-Emitting Diodes. Molecules *24*, 151. https://doi.org/10.3390/molecules24010151.

41. Liao, L.S., Klubek, K.P., and Tang, C.W. (2004). High-efficiency tandem organic light-emitting diodes. Appl. Phys. Lett. *84*, 167–169. https://doi.org/10.1063/1.1638624.

42. Chen, Y., and Ma, D. (2012). Organic semiconductor heterojunctions as charge generation layers and their application in tandem organic light-emitting diodes for high power efficiency. J. Mater. Chem. *22*, 18718–18734. https://doi.org/10.1039/c2jm32246c.

43. Bae, H.W., Kwon, Y.W., An, M., Kim, J., Kwon, J.H., and Lee, D. (2021). High-Color-Stability and Low-Driving-Voltage White Organic Light-Emitting Diodes on Silicon with Interlayers of Thin Charge Generation Units

for Microdisplay Applications. ACS Appl. Electron. Mater. *3*, 3240–3246. https://doi.org/10.1021/acsaelm.1c00406.

44. KOPIN CORPORATION'S OLED MICRODISPLAY SUCCESS HIGHLIGHTED IN INDUSTRY RESEARCH https://www.kopin.com/press-releases/kopin-corporations-oled-microdisplay-success-highlighted-in-industry-research/.
45. Cho, H., Byun, C.-W., Kang, C.-M., Shin, J.-W., Kwon, B.-H., Choi, S., Cho, N.S., Lee, J.-I., Kim, H., Lee, J.H., et al. (2019). White organic light-emitting diode (OLED) microdisplay with a tandem structure. J. Infect. Dis. *20*, 249–255. https://doi.org/10.1080/15980316.2019.1671240.
46. Song, W., You, J., Wu, C.-Y., Wang, L., Shen, Y., Bo, B., Quan, W., Luo, C., Yu, D., Li, W., et al. (2019). 5-3: 3-Stacked Top-Emitting White OLEDs with Super-Wide Color Gamut and High Efficiency. SID Symp. Dig. Tech. Pap. *50*, 46–49. https://doi.org/10.1002/sdtp.12852.
47. Zou, S.-J., Zeng, X.-Y., Li, Y.-Q., and Tang, J.-X. (2021). The Strategies for High-Performance Single-Emissive-Layer White Organic Light-Emitting Diodes. Laser Photon. Rev. *15*, 2000474. https://doi.org/10.1002/lpor.202000474.
48. Hamer, J., Kondakova, M., Spindler, J., Cupello, R., Hamer, S., Andre, M., McClurg, S., Pleten, A., Primerano, B., Scott, D., et al. (2020). High-performance OLED microdisplays made with multi-stack OLED formulations on CMOS backplanes. Proc. SPIE *11473*, 114730F. https://doi.org/10.1117/12.2569848.
49. Qian, Y., Yang, Z., Hsiang, E.-L., Yang, Q., Nilsen, K., Huang, Y.-H., Lin, K.-H., and Wu, S.-T. (2023). Human Eye Contrast Sensitivity to Vehicle Displays under Strong Ambient Light. Crystals *13*, 1384. https://doi.org/10.3390/cryst13091384.
50. Kim, S.K., Park, M.J., Lampande, R., Jung, S.W., Park, H.u., Jeong, J.K., and Kwon, J.H. (2020). Primary color generation from white organic light-emitting diodes using a cavity control layer for AR/VR applications. Org. Electron. *87*, 105938. https://doi.org/10.1016/j.orgel.2020.105938.
51. Joo, W.-J., Kyoung, J., Esfandyarpour, M., Lee, S.-H., Koo, H., Song, S., Kwon, Y.-N., Song, S.H., Bae, J.C., Jo, A., et al. (2020). Metasurface-driven OLED displays beyond 10,000 pixels per inch. Science *370*, 459–463. https://doi.org/10.1126/science.abc8530.
52. Sim, S., Ryu, J., Ahn, D.H., Cho, H., Kang, C.M., Shin, J.-W., Joo, C.W., Kim, G.H., Byun, C.-W., Cho, N.S., et al. (2022). Color gamut change by optical crosstalk in high-resolution organic light-emitting diode microdisplays. Opt Express *30*, 24155–24165. https://doi.org/10.1364/OE.463095.
53. Lee, J.-K., Cho, S., and Kang, D.W. (2016). Analysis of light leakage between the adjacent pixels in a color-filter stacked white OLED display. Displays *45*, 6–13. https://doi.org/10.1016/j.displa.2016.09.001.
54. Diethelm, M., Penninck, L., Altazin, S., Hiestand, R., Kirsch, C., and Ruhstaller, B. (2018). Quantitative analysis of pixel crosstalk in AMOLED displays. J. Infect. Dis. *19*, 61–69. https://doi.org/10.1080/15980316.2018.1428232.
55. Kim, C., Kim, K., Kwon, O., Jung, J., Park, J.K., Kim, D.H., and Jung, K. (2020). Fine metal mask material and manufacturing process for high-resolution active-matrix organic light-emitting diode displays. J. Soc. Inf. Disp. *28*, 668–679. https://doi.org/10.1002/jsid.901.
56. Lim, J.H., Park, E.C., Lee, S.Y., Yoon, J.-W., Ha, S.-S., Joo, J., Lee, H.-J., Jung, S.-B., and Song, K. (2007). Fabrication of Ni Metal Mask by Electroforming Process Using Wetting Agents. J. Electron. Mater. *36*, 1510–1515. https://doi.org/10.1007/s11664-007-0211-8.
57. Jung, J.H., Kim, C., Sung, D.Y., Park, J.S., Kim, T., Park, J.K., Kim, D.H., and Jung, K. (2021). 55.3: Invited Paper: RGB side-by-side OLED Microdisplay Technology. SID Symp. Dig. Tech. Pap *52*, 660–663. https://doi.org/10.1002/sdtp.15240.
58. Jung, J.H., Choi, M.H., Kang, M., Kwon, O.E., Kim, C., and Jung, K. (2023). 17-5: Enhancement of Luminance Efficiency of 3,000ppi OLED Microdisplay using RGB Direct Patterning. SID Symp. Dig. Tech. Pap. *54*, 217–220. https://doi.org/10.1002/sdtp.16529.
59. Kweon, H., Choi, K.-Y., Park, H.W., Lee, R., Jeong, U., Kim, M.J., Hong, H., Ha, B., Lee, S., Kwon, J.-Y., et al. (2022). Silicone engineered anisotropic lithography for ultrahigh-density OLEDs. Nat. Commun. *13*, 6775. https://doi.org/10.1038/s41467-022-34531-y.
60. World's First Maskless Deposition + Lithographic OLED https://www.eleap.jp/.
61. Saito, T., Mizuguchi, T., Okamoto, Y., Ito, M., Toyotaka, K., Kozuma, M., Matsuzaki, T., Kobayashi, H., Onuki, T., Hiura, Y., et al. (2022). 10-1: Layout of 1.50-inch, 3207-ppi OLED Display with OSLSI/SiLSI Structure Capable of Division Driving Fabricated through VLSI Process with Side-by-Side Patterning by Photolithography. SID Symp. Dig. Tech. Pap. *53*, 94–97. https://doi.org/10.1002/sdtp.15425.
62. Kim, K., Kim, G., Lee, B.R., Ji, S., Kim, S.-Y., An, B.W., Song, M.H., and Park, J.-U. (2015). High-resolution electrohydrodynamic jet printing of small-molecule organic light-emitting diodes. Nanoscale *7*, 13410–13415. https://doi.org/10.1039/C5NR03034J.
63. Mu, L., Jiang, C., Wang, J., Zheng, H., Ying, L., Xu, M., Wang, J., Peng, J., and Cao, Y. (2020). 34-3: OLED Display with High Resolution Fabricated by Electrohydrodynamic Printing. SID Symp. Dig. Tech. Pap. *51*, 485–488. https://doi.org/10.1002/sdtp.13911.
64. Cho, T.-Y., Lin, C.-L., and Wu, C.-C. (2006). Microcavity two-unit tandem organic light-emitting devices having a high efficiency. Appl. Phys. Lett. *88*, 111106. https://doi.org/10.1063/1.2185077.
65. Fu, X., Yin, S., Chen, Y.-A., Zhu, L., Dong, Q., Chang, C.-H., and So, F. (2021). Light extraction in tandem organic light emitting diodes. Appl. Phys. Lett. *119*, 060504. https://doi.org/10.1063/5.0057325.
66. Dong, Q., Zhu, L., Yin, S., Lei, L., Gundogdu, K., and So, F. (2023). High-Efficiency Linearly Polarized Organic Light-Emitting Diodes. ACS Photonics *10*, 3342–3349. https://doi.org/10.1021/acsphotonics.3c00812.
67. Lupton, J.M., Matterson, B.J., Samuel, I.D.W., Jory, M.J., and Barnes, W.L. (2000). Bragg scattering from periodically microstructured light emitting diodes. Appl. Phys. Lett. *77*, 3340–3342. https://doi.org/10.1063/1.1320023.
68. Fu, X., Mehta, Y., Chen, Y.-A., Lei, L., Zhu, L., Barange, N., Dong, Q., Yin, S., Mendes, J., He, S., et al. (2021). Directional Polarized Light Emission from Thin-Film Light-Emitting Diodes. Adv. Mater. *33*, 2006801. https://doi.org/10.1002/adma.202006801.
69. Kim, J.-B., Lee, J.-H., Moon, C.-K., Kim, K.-H., and Kim, J.-J. (2015). Highly enhanced light extraction from organic light emitting diodes with little image blurring and good color stability. Org. Electron. *17*, 115–120. https://doi.org/10.1016/j.orgel.2014.12.006.
70. Kim, J., Qu, Y., Coburn, C., and Forrest, S.R. (2018). Efficient Outcoupling of Organic Light-Emitting Devices Using a Light-Scattering Dielectric Layer. ACS Photonics *5*, 3315–3321. https://doi.org/10.1021/acsphotonics.8b00539.
71. Jeong, C., Park, Y.-B., and Guo, L.J. (2021). Tackling light trapping in organic light-emitting diodes by complete elimination of waveguide modes. Sci. Adv. *7*, eabg0355. https://doi.org/10.1126/sciadv.abg0355.
72. Ding, Y., Luo, Z., Borjigin, G., and Wu, S.-T. (2024). Breaking the efficiency limit of pancake optics in virtual reality. Proc. SPIE *12913*, 1291309. https://doi.org/10.1117/12.3009374.
73. Ding, Y., Luo, Z., Borjigin, G., and Wu, S.-T. (2024). Breaking the optical efficiency limit of virtual reality with a nonreciprocal polarization rotator. Opto-Electron. Adv. *7*, 230178. https://doi.org/10.29026/oea.2024.230178.
74. Geng, M., Gollier, J., Wheelwright, B.M., Peng, F., Sulai, Y., Lewis, B., Chan, N., Lam, W.S.T., Fix, A., Lanman, D., et al. (2018). Viewing optics for immersive near-eye displays: pupil swim/size and weight/stray light. Proc. SPIE *10676*, 1067606. https://doi.org/10.1117/12.2307671.
75. Hou, Q., Cheng, D., Li, Y., Zhang, T., Li, D., Huang, Y., Chen, H., Wang, Q., Hou, W., Yang, T., and Wang, Y. (2022). Stray light analysis and suppression method of a pancake virtual reality head-mounted display. Opt Express *30*, 44918–44932. https://doi.org/10.1364/OE.476078.

76. Hao, B., Le, J.D., Aastuen, D.J.W., Kotz, A.L., McGrath, K.A., and Kent, S. (2023). Ghost analysis of a polarized catadioptric system for virtual reality. Proc. SPIE *12449*, 124490U. https://doi.org/10.1117/12.2648497.

77. Le, J.D., Hao, B., Aastuen, D.J.W., Kent, S., Kotz, A.L., O'Neill, M., Huynh, K., Dachel, M., and McGrath, K.A. (2023). High resolution reflective polarizer lens for catadioptric VR optics with accommodating eye box design. Proc. SPIE *12449*, 124490O. https://doi.org/10.1117/12.2647908.

78. Li, Y., Zhan, T., Yang, Z., Xu, C., LiKamWa, P.L., Li, K., and Wu, S.-T. (2021). Broadband cholesteric liquid crystal lens for chromatic aberration correction in catadioptric virtual reality optics. Opt Express *29*, 6011–6020. https://doi.org/10.1364/OE.419595.

79. Chen, W.T., Zhu, A.Y., Sanjeev, V., Khorasaninejad, M., Shi, Z., Lee, E., and Capasso, F. (2018). A broadband achromatic metalens for focusing and imaging in the visible. Nat. Nanotechnol. *13*, 220–226. https://doi.org/10.1038/s41565-017-0034-6.

80. Luo, Z., Li, Y., Semmen, J., Rao, Y., and Wu, S.-T. (2023). Achromatic diffractive liquid-crystal optics for virtual reality displays. Light Sci. Appl. *12*, 230. https://doi.org/10.1038/s41377-023-01254-8.

81. Zhan, T., Zou, J., Xiong, J., Liu, X., Chen, H., Yang, J., Liu, S., Dong, Y., and Wu, S.-T. (2020). Practical Chromatic Aberration Correction in Virtual Reality Displays Enabled by Cost-Effective Ultra-Broadband Liquid Crystal Polymer Lenses. Adv. Opt. Mater. *8*, 1901360. https://doi.org/10.1002/adom.201901360.

82. Usukura, N., Minoura, K., and Maruyama, R. (2023). Novel pancake-based HMD optics to improve light efficiency. J. Soc. Inf. Disp. *31*, 344–354. https://doi.org/10.1002/jsid.1212.

83. Luo, Z., Ding, Y., Rao, Y., and Wu, S.-T. (2023). High-efficiency folded optics for near-eye displays. J. Soc. Inf. Disp. *31*, 336–343. https://doi.org/10.1002/jsid.1207.

84. Karki, D., Stenger, V., Pollick, A., and Levy, M. (2017). Thin-film magnetless Faraday rotators for compact heterogeneous integrated optical isolators. J. Appl. Phys. *121*, 233101. https://doi.org/10.1063/1.4986237.